

Pixelated transmission-mode diamond X-ray detector

Tianyi Zhou,^a Wenxiang Ding,^b Mengjia Gaowei,^c Gianluigi De Geronimo,^c Jen Bohon,^d John Smedley^c and Erik Muller^{e*}

Received 14 April 2015
Accepted 7 August 2015

Edited by P. A. Pianetta, SLAC National Accelerator Laboratory, USA

Keywords: X-ray detector; beam position monitor; flux; morphology; diamond.

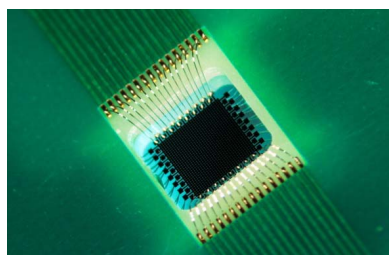
^aMaterial Science and Engineering, Stony Brook University, Stony Brook, NY 11790, USA, ^bElectrical and Computer Engineering, Stony Brook University, Stony Brook, NY 11790, USA, ^cInstrumentation Division, Brookhaven National Laboratory, Upton, NY 11973, USA, ^dCenter for Synchrotron Biosciences, Case Western Reserve University, Upton, NY 11973, USA, and ^ePhysics and Astronomy, Stony Brook University, Stony Brook, NY 11790, USA.

*Correspondence e-mail: erik.muller@stonybrook.edu

Fabrication and testing of a prototype transmission-mode pixelated diamond X-ray detector (pitch size 60–100 μm), designed to simultaneously measure the flux, position and morphology of an X-ray beam in real time, are described. The pixel density is achieved by lithographically patterning vertical stripes on the front and horizontal stripes on the back of an electronic-grade chemical vapor deposition single-crystal diamond. The bias is rotated through the back horizontal stripes and the current is read out on the front vertical stripes at a rate of ~ 1 kHz, which leads to an image sampling rate of ~ 30 Hz. This novel signal readout scheme was tested at beamline X28C at the National Synchrotron Light Source (white beam, 5–15 keV) and at beamline G3 at the Cornell High Energy Synchrotron Source (monochromatic beam, 11.3 keV) with incident beam flux ranges from 1.8×10^{-2} to 90 W mm^{-2} . Test results show that the novel detector provides precise beam position (positional noise within 1%) and morphology information (error within 2%), with an additional software-controlled single channel mode providing accurate flux measurement (fluctuation within 1%).

1. Introduction

Many synchrotron-based technologies, as they are developed to take advantage of next-generation synchrotron sources, are trending toward use of high-flux beams and/or beams which require enhanced stability and precise understanding of beam position and intensity from the front end of the beamline all the way to the sample. Major challenges for these beamlines include: (a) heat load management; (b) real-time volumetric measurement of beam properties; (c) feedback and control systems for optical elements or sample positioning stages. No single current technology can address all of these challenges. Diamond has some prominent properties that make it a promising candidate as the next-generation transmission X-ray detector (Berdermann *et al.*, 2010; Bergonzo *et al.*, 2000; Bohon *et al.*, 2010; Kagan, 2005a,b; Keister & Smedley, 2009; Muller *et al.*, 2012; Shu *et al.*, 1999), such as low X-ray absorption, high thermal conductivity, high mechanical strength, radiation hardness, a wide indirect band gap, and high carrier velocity for both electrons and holes. In recent years, synthetic single-crystal diamond of sufficient quality (low nitrogen, few to no electrically active defects) has become reasonably available to enable development of this technology. Diamond detectors have significantly less X-ray absorption than Si detectors with the same thickness and, at thicknesses of less than 50 μm , become competitive with



© 2015 International Union of Crystallography

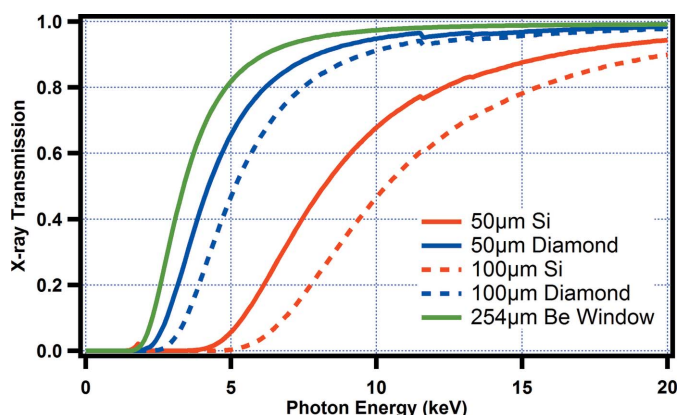


Figure 1
X-ray transmission of Si and diamond (Henke *et al.*, 1993); the absorption of a 60 nm platinum electrode is included. The absorption of a standard beryllium window is shown for reference.

standard Be windows for transmission. Fig. 1 shows a diagram of beam transmission *versus* photon energy, which compares the transmission curves for diamond, silicon and a beryllium window. Several single-channel and quadrant diamond X-ray flux and/or position detectors have been successfully fabricated for use in various synchrotron beamlines. In this paper, the development of a pixelated diamond detector prototype is described. It is aimed to provide accurate real-time position, flux and morphology for high-flux X-ray beams.

2. Materials and methods

2.1. Detector fabrication

The detectors were fabricated beginning with commercially available high-purity single-crystal (001) diamonds grown by chemical vapor deposition (CVD) with less than 5 ppb nitrogen impurity. The diamond plates were acquired from two different vendors, IIA Technologies (IIA; Singapore) and Element Six (E6; Santa Clara, CA, USA), and subsequently sliced and polished by Applied Diamond (Wilmington, DE, USA). The diamonds were screened using birefringence imaging and X-ray topography to select diamonds with the

fewest dislocation bundles, defects which result in photoconductive gain (Muller *et al.*, 2009). The X-ray topography was performed at the National Synchrotron Light Source (NSLS) beamline X19C; the diamond (022) reflection is shown for detector-qualified and unqualified diamonds in Fig. 2 [panels (a) and (d), respectively]. These diamonds exhibit three main types of defects: growth dislocations lying on the [001] axis, dislocation bundles, and slip bands of {111}(110) and (110) slip systems (Gaukroger *et al.*, 2008). Diamonds exhibiting localized very high strain regions, such as dislocation bundles emanating from an inclusion [which form a characteristic 'x' shape in the topograph (Pinto & Jones, 2009)], are to be avoided. Together with birefringence imaging [Figs. 2(b) and 2(c)], which is also sensitive to the high strain field from inclusions, we have selected diamonds relatively free of inclusion defects. Fig. 2(b) shows the birefringence image of a diamond obtained from E6 (used to fabricate a 16-pixel detector), with characteristically low dislocation density. Fig. 2(c) shows the birefringence image of a diamond obtained from IIA used in the fabrication of a 1024-pixel detector, which demonstrates a relatively high but uniform dislocation density without any potentially electrical active defects. It has previously been shown that defects may reduce carrier mobility in diamond (Lohstroh *et al.*, 2007), thus we expect a lower carrier saturation voltage for the E6 diamond due to the lower dislocation density.

Four pixelated detectors have been fabricated and tested, two with 16 effective pixels and two with 1024 effective pixels. The 16-pixel detectors demonstrated proof-of-principal; however, this article will concentrate on the results from the 1024-pixel detectors.

The polished diamond plates were ultrasonically cleaned in acetone followed by 2-propanol and DI water, then exposed to a UV lamp in air for 4 h per side. In addition to removing adventitious carbon, this establishes a robust oxygen termination on the diamond, which has been shown to reduce or eliminate non-uniformities in the device response due to photoconductive gain by maintaining a high Schottky barrier (Gaowei *et al.*, 2012). The 32-stripe pattern was created on the diamond surface following standard lithography procedures: (a) spin photoresist, Microposit S1805 at 6000 rpm; (b) bake at

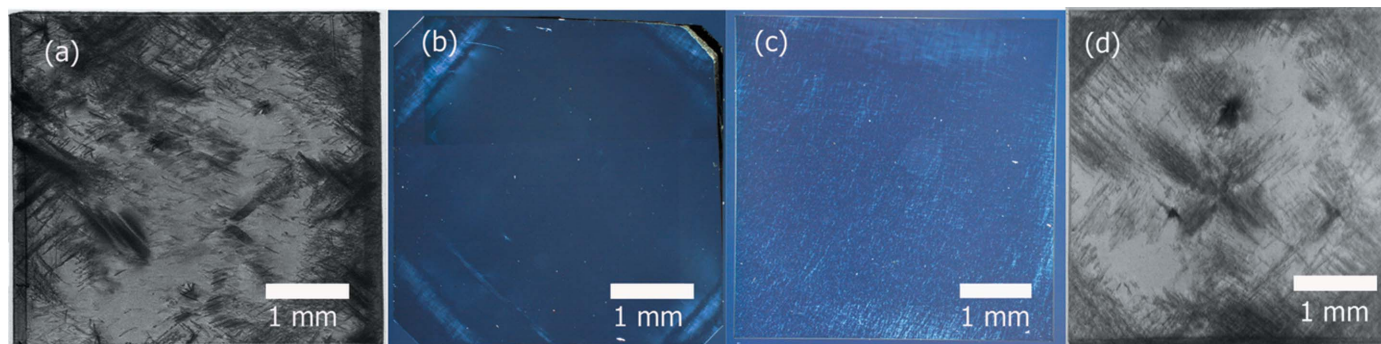


Figure 2
(a) White-beam X-ray topography of the (022) reflection of E6 diamond used for the 16-pixel detector; (b) birefringence image of E6 diamond used for the 16-pixel detector; (c) birefringence image of IIA diamond used for the 1024-pixel detector; (d) white-beam X-ray topography of the (220) reflection of an unqualified diamond due to several electrical active defects in the center area.

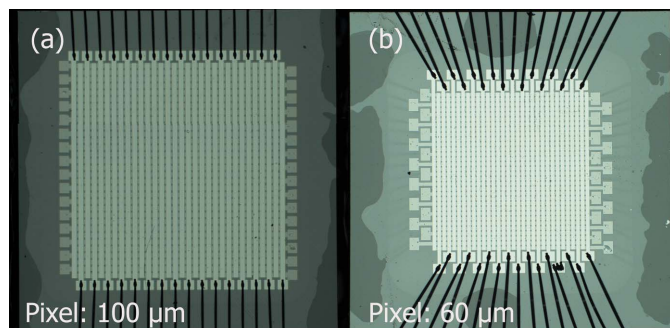


Figure 3 32-stripe electrode pattern on (a) the 4.7 mm × 4.7 mm IIA diamond and (b) the 3.8 mm × 3.8 mm E6 diamond.

373 K for 3 min; (c) mask alignment and UV exposure for 12 s; (d) develop in Microposit MF312 solution for 2 min. Platinum contacts, 25 nm thick, were then sputter-coated onto the diamond surface, followed by lift-off in acetone to reveal the desired electrode pattern. The diamond was then turned over for the identical pattern, rotated 90°, to be placed on the back side.

The stripe pattern used in these detectors is shown in Fig. 3. Detector 1 (using the IIA diamond) has an overall dimension of 4.7 mm × 4.7 mm × 0.05 mm. The pattern consists of 32 stripes, each 80 µm wide with a separation of 20 µm, yielding a pitch of 100 µm. The active area of this device is 3.21 mm × 3.21 mm (10.3 mm²) consisting of 1024 effective pixels. Detector 2 (using the E6 diamond) has overall dimensions of 3.8 mm × 3.8 mm × 0.05 mm. In this case, each stripe is 45 µm wide with a separation of 15 µm, yielding a pitch of 60 µm. The active area of this device is 1.905 mm × 1.905 mm (3.63 mm²), also consisting of 1024 effective pixels. Each diamond was fixed to a custom circuit board with non-conductive epoxy; each stripe was wire bonded to traces on the circuit board using one 25 µm-thick aluminium wire. Connections to the circuit boards were made with standard D-Sub connectors.

2.2. Readout electronics

An image is acquired by cycling the high voltage applied to each stripe on one side of the detector and measuring the current on all stripes on the opposite side simultaneously. Following the diagram in Fig. 4(a), the cycled bias is applied to the horizontal stripes one at a time, thereby encoding the vertical position. The stripes that are not biased are placed in an ‘off’ state, which is a small non-zero bias explained in more detail in the calibration section of this article. The current is measured in parallel on all of the vertical stripes, encoding the horizontal position. Since only one row is active at a time, the ohmic heat generated in this case is minimized (Muller *et al.*, 2012). The architecture of the readout electronics is shown in Fig. 4(b). Each analog channel has its own low-noise trans-impedance amplifier for the conversion of the current signal from the sensor into a voltage signal. The amplifier is followed by a low-pass RC filter to optimize the signal-to-noise ratio; the filtered voltage signal is then sampled and digitized by an analog-to-digital converter (ADC). A field-programmable gate array (FPGA) is responsible for reading out the data from the ADC and synchronizing the ADC with the high-voltage switching.

Commercial components were selected to realise the low-noise front-end and the high-voltage switching circuits. To switch the ~40 V bias voltage required for full carrier collection in the IIA diamond as rapidly as possible, we chose one of the fastest multi-channel high-voltage analog switches currently available, HV2701 from Supertex Inc., capable of achieving a maximum channel switching frequency of 200 kHz. However, a settling time is required for the sensor after the application of the high voltage and for the output of the RC filter to settle before the ADC can sample the signal. Given the RC filter time constant of 47 µs, a 300 µs delay time is conservatively applied after the high-voltage switching before the ADC samples the signal. In addition, 700 µs is given to allow the ADC to sample several times. Therefore, a total of 1 ms is taken for each bias stripe cycle. This leads to an image sampling time of 32 ms and a sampling rate of ~30 Hz,

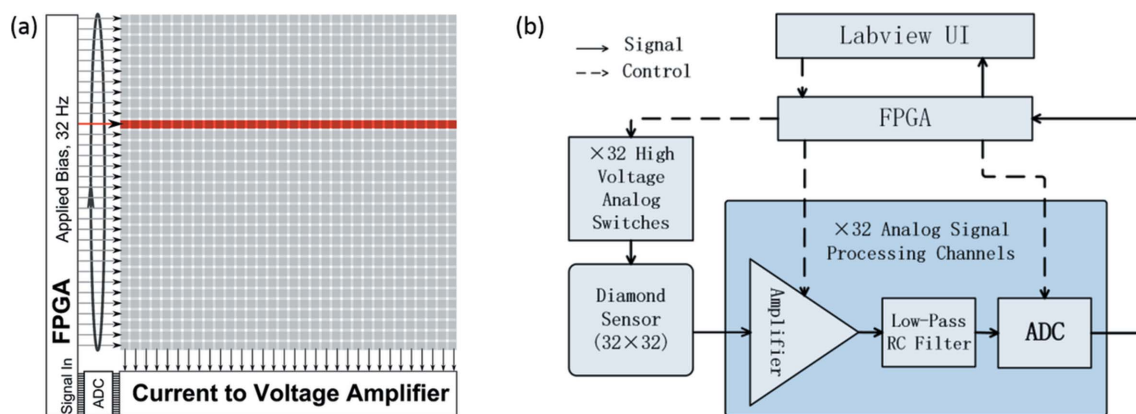


Figure 4 (a) Sketch of the readout electronics connected to the sensor. (b) Block diagram illustrating the readout electronics, which consists of 32-channel high-voltage analog switches, 32 low-noise front-end channels and an FPGA control system.

which could be further increased by reducing the RC delay time and ADC sampling during a cycle. The 32 analog channels consist of 16 two-channel transimpedance amplifiers and two 16-channel ADCs; the use of multi-channel Op-Amps to realise the transimpedance amplifiers and multi-channel ADCs makes the board more compact (PC board size: 7.4" × 10.0"). To minimize the power consumption, the supply voltage for each Op-Amp and ADC is chosen to be 3.3 V. An external reference voltage of 2.5 V is applied to the ADCs. The ADC resolution is 12-bits. The ADC sampling rate for each channel is adjustable from 0.625 to 100 ksp/s (ksp/s = kilo samples per second), which satisfies the ~30 Hz bias switching scheme. Each analog channel can read current signals in the range 20 nA to 140 mA for both positive and negative polarity. A separate custom FPGA board was used to realise the control of the ADCs and high-voltage switching, obtain data from the ADCs and communicate with the computer hosting the user interface. A custom National Instruments LabVIEW software interface was designed to continuously display the image of the X-ray beam. An EPICS-based user interface is currently being developed to integrate the system into the EPICS control systems at NSLS-II.

3. Experiment and results

3.1. Experimental setup

The performance of the X-ray detectors was evaluated at beamline X28C at the NSLS and at beamline G3 of the Cornell High Energy Synchrotron Source (CHESS). The NSLS X28C beamline consists of a toroidally focused white beam (5–15 keV) from a bending magnet source (Sullivan *et al.*, 2008). The experimental setup at X28C is shown in Fig. 5. Two apertures were installed on a translation stage which allowed the selection of three beam sizes: a 1.6 mm-diameter pinhole, a 100 μm pinhole and no aperture. Without an aperture, the beam size is determined by the focusing parameters used for the toroidal mirror. The imaging detector was mounted downstream of the pinhole on an x - z translation stage, with a calibrated quadrant diamond X-ray beam position monitor mounted directly in line on the same stage for

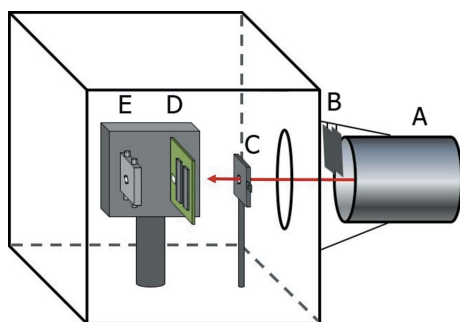


Figure 5
Schematic of the experiment setup at X28C, NSLS. A is the beam exit from the synchrotron ring; B indicates Al attenuators; C is the pinhole to define beam size; D is the pixelated detector; E is the pre-calibrated diamond detector.

simultaneous measurement. Aluminium filters of several different thicknesses were placed into the beam upstream of the apertures to provide controlled changes in beam flux. The experimental setup was enclosed in a nitrogen-filled box to avoid ozone corrosion of contacts. Experiments at CHESS G3 (monochromatic 11.2 keV beam from an undulator source) were also performed in a similar manner; however, the beam size was controlled by slits rather than by apertures and the calibrated reference detector was upstream of the imaging device for these tests.

3.2. Detector functionality tests

The first tests were to determine the optimal operating voltage and uniformity of the detectors. For this test, each detector was effectively converted into a single-channel X-ray flux monitor by electrically connecting all 32 stripes on each side, applying bias to one side and reading current from the other. The high-flux X-ray beam passed through a 330 μm aluminium filter and was defined by a 1.6 mm aperture prior to the detector to protect wire bonds from the direct full flux beam. With the X-rays incident on the detector, the bias on the X-ray incident side was scanned and the current collected by a Keithley electrometer (model 6517A) on the exit side with the results shown in Fig. 6. As expected, the E6 diamond shows a quick rise to full collection (0.5 V) and no evidence of photoconductive gain; however, the IIa diamond required significantly higher bias to receive full collection (40 V) and photoconductive gain was observed in the negative polarity. It

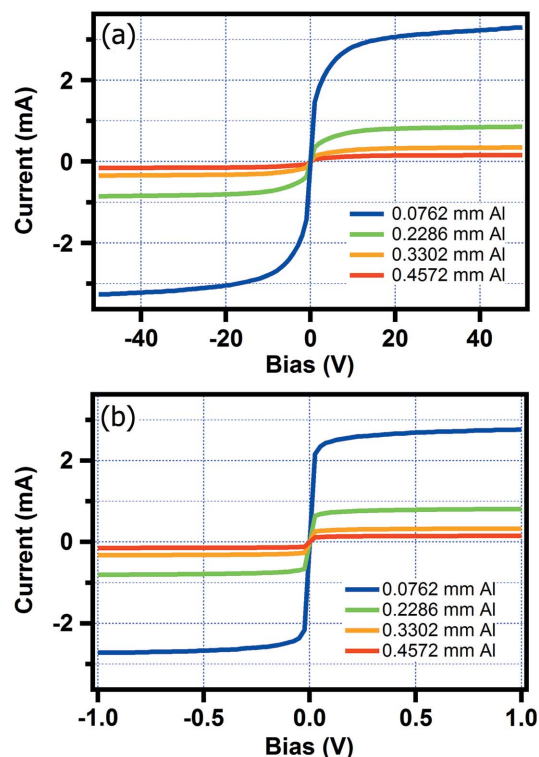


Figure 6
Bias scan diagram of (a) the IIa diamond detector, 50 μm thick, and (b) the E6 diamond detector, 50 μm thick.

should be noted that, as the flux was increased (by removing the Al filters), the effect of the photoconductive gain was less prominent, indicating that its contribution is localized.

The detector and electronics were reconfigured to imaging mode to determine the flux, position and morphology performance of the two detectors. The input current amplifiers operate with a virtual ground which has been raised to individually adjustable bias near ~ 1.25 V; this allows some bipolar performance, but requires the bias stripes to also be raised to ~ 1.25 V to turn those channels off. As can be seen in Fig. 6, the current is very sensitive to the bias for the channels which are ‘turned off’, requiring very careful adjustment to ensure that each input amplifier is raised to identical bias. Failure to perform this bias leveling results in significant signal from any stripe where there is incident X-ray beam. This effect is more significant for the E6 detector as it achieves full collection at lower electric field. Once this bias is leveled, the detectors performed similarly. In the subsequent set of experiments run at CHESS, a mechanism was devised to alleviate the need for fine-tuning of the ground bias in the case of the detector fabricated using the higher quality diamond. Rather than attempting to compensate for small differences in the amplifier bias values for each channel (due to manufacturing differences in the amplifiers), for one readout scan all channels were biased to -1.25 V, then in a subsequent readout scan the channel of interest was set to 10 V while the others remained at -1.25 V, with software subtraction of the values measured from the previous scan. This resulted in clean image backgrounds (Fig. 7a) for observation of the beam morphology.

The beam position was monitored as the detector was scanned in both the vertical and horizontal directions. Both detectors behaved as expected and the images are shown in Fig. 7. Accompanying the images is a plot of the flux (sum of the pixels) on both horizontal and vertical lines with the maximum peak width. The detected beam size in the horizontal direction is 1.5 ± 0.05 mm and it is 1.4 ± 0.05 mm vertically, while the beam size defined by the pinhole is 1.6 mm in diameter. Note that the pitch size for the IIa diamond detector is $100 \mu\text{m}$. Because of charge sharing between pixels, similar to the operation of a quadrant position monitor, the position can be determined with higher precision than an individual pixel. Although the flux is constant, as expected, the

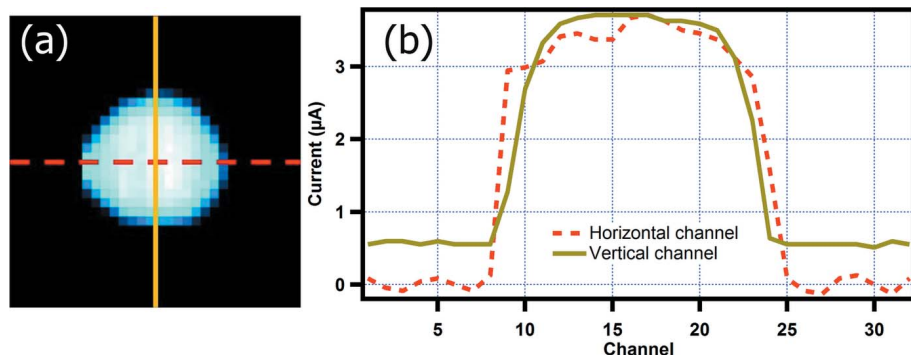


Figure 7
(a) 1.6 mm-diameter beam on the IIa diamond detector; (b) line profile of both vertical and horizontal lines with the maximum peak width.

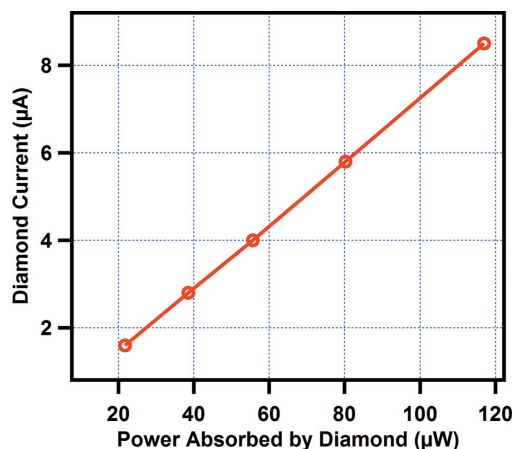


Figure 8
Response calibration of the pixelated detector in flux mode, $w = 13.6 \pm 0.2$ eV, measured at the G3 beamline at CHESS. $R^2 = 0.999$.

magnitude is consistently about three times larger than expected based on the calibrated flux. This can be qualitatively understood as the stray electric field between the active stripe and the current readout stripe. In general, the electric field required for full collection for diamond is $\sim 0.05 \text{ V } \mu\text{m}^{-1}$; any charge carrier created in this region will be collected by the current readout stripe, resulting in a larger effective width of the pixel. To accurately measure the flux, the detector switches to a ‘flux’ mode where all of the bias channels are simultaneously switched ‘on’ and the current from all of the readout channels is summed. This sum corresponds to the response that the detector would have if it were a single channel diode. The comparison of this flux reading against the flux as simultaneously measured by a calibrated detector in line is shown in Fig. 8. The detector switches to this mode ~ 30 times per second.

The morphology of the beam while changing the focus condition of the toroidal mirror was also tested. The 1.6 mm aperture was removed to allow the detector to be illuminated by the full extent of the beam which was 2.5 mm in diameter in the unfocused condition. Note that the $330 \mu\text{m}$ aluminium filter was not used during the morphology test, thus the flux value is around ten times greater than that used for the positional measurement. Fig. 9 shows a comparison of the beam morphology as collected by the diamond imaging detector with images of the beam collected on burn paper. The beam can also be observed to hit the wire bonds, showing a high intensity in the image; these pixels have less than 10% effect on the total calculated flux, and will be masked in the final device to avoid this.

4. Conclusions

We have demonstrated the feasibility of building a pixelated transmission-mode CVD diamond X-ray detector, which

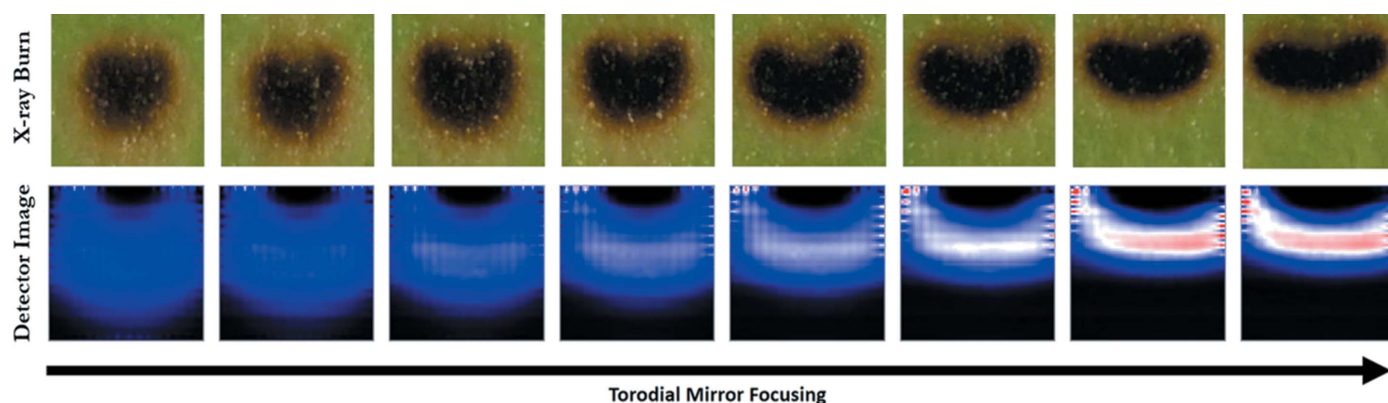


Figure 9
Burn paper image and detected beam shape for different focus levels.

measures beam flux, position and morphology in real time. Diamonds were selected by X-ray topography and birefringence imaging and fabricated into four imaging detectors. Two of these detectors had 1024 (32×32) 'pixels' and have been shown to faithfully reproduce the X-ray beam profile produced by two synchrotron beamlines. The effect of adjusting toroidal focusing and of varying upstream slit dimensions was observed with these detectors, and the morphology of the beam corresponds well to the expected shapes. This was achieved using a novel readout scheme, in which current signal is collected from the front stripes while bias is rotated through the back stripes at a rate of up to 1 kHz, providing imaging at ~ 30 Hz. The detector uses a 'flux' mode interleaved with the imaging mode to produce accurate flux measurement over a large dynamic range. Diamond detectors with a greater active area are possible if large electrical grade diamonds become commercially available.

A standalone imaging detector has been developed; the project will now continue with the incorporation of this device into a vacuum window, which will act as a vacuum–air interface at the beam exit while simultaneously measuring flux, position and morphology of the beam. The current work has successfully demonstrated the imaging capability that will be integrated into this device, along with the electronics for the device readout. Provided the per-pixel current response in the diamond is sufficient to be measured with our electronics (~ 20 nA or higher), this device will provide an accurate beam diagnostic across a wide range of energies. Ongoing studies include diamond brazing techniques for integration into the vacuum window, robust blocking contacts under high temperature, a higher-speed readout system, measurement of lower-flux monochromatic beams and a user-friendly interface.

Acknowledgements

The authors wish to thank Donald Abel and John Walsh for design and fabrication of sample mounts, Abdul Rumaiz for mask aligner support, Ming Lu for assistance in metallization and Donald Pinelli for wirebonding work. We would like to thank the Instrumentation Division (BNL) for the design and

fabrication of printed circuit boards. The authors would also like to thank all of the NSLS and CHESS staff for their assistance at the beamlines and CFN staff for assistance in the clean room. The authors wish to acknowledge the support by the National Science Foundation Division of Biological Infrastructure Instrument Development for Biological Research Program under DBI-1255340, DBI-1254804 and DBI-1254587 as well as NSF DBI-1228549. Use of the Case Center for Synchrotron Biosciences is supported by the National Institute of Biomedical Imaging and Bioengineering under P30-EB-009998. Use of the National Synchrotron Light Source, Brookhaven National Laboratory, was supported by the US Department of Energy, Office of Science, Office of Basic Energy Sciences, under contract No. DE-AC02-98CH10886. Use of CHESS is supported by the NSF and NIH/NIGMS via NSF award DMR-1332208.

References

- Berdermann, E., Pomorski, M., de Boer, W., Ciobanu, M., Dunst, S., Grah, C., Kiš, M., Koenig, W., Lange, W., Lohmann, W., Lovrinčić, R., Moritz, P., Morse, J., Mueller, S., Pucci, A., Schreck, M., Rahman, S. & Träger, M. (2010). *Diamond Relat. Mater.* **19**, 358–367.
- Bergonzo, P., Brambilla, A., Tromson, D., Mer, C., Hordequin, C., Guizard, B., Foulon, F., Solé, V. A. & Gauthier, C. (2000). *Diamond Relat. Mater.* **9**, 960–964.
- Bohon, J., Muller, E. & Smedley, J. (2010). *J. Synchrotron Rad.* **17**, 711–718.
- Gaowei, M., Muller, E. M., Rumaiz, A. K., Weiland, C., Cockayne, E., Jordan-Sweet, J., Smedley, J. & Woicik, J. C. (2012). *Appl. Phys. Lett.* **100**, 201606.
- Gaukroger, M., Martineau, P., Crowder, M., Friel, I., Williams, S. & Twitchen, D. (2008). *Diamond Relat. Mater.* **17**, 262–269.
- Henke, B. L., Gullikson, E. M. & Davis, J. C. (1993). *At. Data Nucl. Data Tables*, **54**, 181–342.
- Kagan, H. (2005a). *Nucl. Instrum. Methods Phys. Res. A*, **541**, 221–227.
- Kagan, H. (2005b). *Nucl. Instrum. Methods Phys. Res. A*, **546**, 222–227.
- Keister, J. W. & Smedley, J. (2009). *Nucl. Instrum. Methods Phys. Res. A*, **606**, 774–779.
- Lohstroh, A., Sellin, P., Wang, S., Davies, A., Parkin, J., Martin, R. & Edwards, P. (2007). *Appl. Phys. Lett.* **90**, 102111.

- Muller, E. M., Smedley, J., Bohon, J., Yang, X., Gaowei, M., Skinner, J., De Geronimo, G., Sullivan, M., Allaire, M., Keister, J. W., Berman, L. & Héroux, A. (2012). *J. Synchrotron Rad.* **19**, 381–387.
- Muller, E. M., Smedley, J., Raghathamachar, B., Gaowei, M., Keister, J. W., Ben-Zvi, I., Dudley, M. & Wu, Q. (2009). *MRS Proc.* **1203**, 1203-J17-19.
- Pinto, H. & Jones, R. (2009). *J. Phys. Condens. Matter*, **21**, 364220.
- Shu, D., Job, P. K., Barraza, J., Cundiff, T. & Kuzay, T. M. (1999). *Proceedings of the 1999 IEEE Particle Accelerator Conference*, 29 March–2 April 1999, New York, USA, pp. 2090–2092.
- Sullivan, M. R., Rekhi, S., Bohon, J., Gupta, S., Abel, D., Toomey, J. & Chance, M. R. (2008). *Rev. Sci. Instrum.* **79**, 025101.